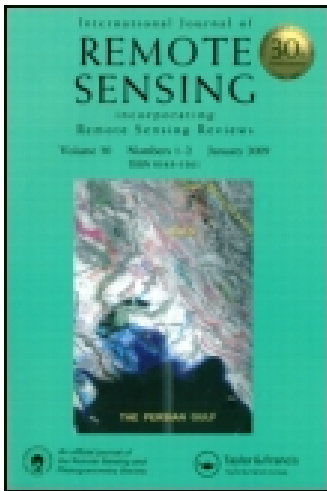


This article was downloaded by: [European Space Agency]

On: 29 July 2014, At: 08:07

Publisher: Taylor & Francis

Informa Ltd Registered in England and Wales Registered Number: 1072954 Registered office: Mortimer House, 37-41 Mortimer Street, London W1T 3JH, UK



International Journal of Remote Sensing

Publication details, including instructions for authors and subscription information:

<http://www.tandfonline.com/loi/tres20>

PROBA-V mission for global vegetation monitoring: standard products and image quality

Wouter Dierckx^a, Sindy Sterckx^a, Iskander Benhadj^a, Stefan Livens^a, Geert Duhoux^a, Tanja Van Achteren^a, Michael Francois^b, Karim Mellab^b & Gilbert Saint^b

^a Flemish Institute for Technological Research (VITO) - Remote Sensing Unit, Boeretang 200, 2400 Mol, Belgium

^b ESA-ESTEC, Noordwijk, The Netherlands

Published online: 27 Mar 2014.

To cite this article: Wouter Dierckx, Sindy Sterckx, Iskander Benhadj, Stefan Livens, Geert Duhoux, Tanja Van Achteren, Michael Francois, Karim Mellab & Gilbert Saint (2014) PROBA-V mission for global vegetation monitoring: standard products and image quality, *International Journal of Remote Sensing*, 35:7, 2589-2614, DOI: [10.1080/01431161.2014.883097](https://doi.org/10.1080/01431161.2014.883097)

To link to this article: <http://dx.doi.org/10.1080/01431161.2014.883097>

PLEASE SCROLL DOWN FOR ARTICLE

Taylor & Francis makes every effort to ensure the accuracy of all the information (the "Content") contained in the publications on our platform. However, Taylor & Francis, our agents, and our licensors make no representations or warranties whatsoever as to the accuracy, completeness, or suitability for any purpose of the Content. Any opinions and views expressed in this publication are the opinions and views of the authors, and are not the views of or endorsed by Taylor & Francis. The accuracy of the Content should not be relied upon and should be independently verified with primary sources of information. Taylor and Francis shall not be liable for any losses, actions, claims, proceedings, demands, costs, expenses, damages, and other liabilities whatsoever or howsoever caused arising directly or indirectly in connection with, in relation to or arising out of the use of the Content.

This article may be used for research, teaching, and private study purposes. Any substantial or systematic reproduction, redistribution, reselling, loan, sub-licensing, systematic supply, or distribution in any form to anyone is expressly forbidden. Terms &

Conditions of access and use can be found at <http://www.tandfonline.com/page/terms-and-conditions>

PROBA-V mission for global vegetation monitoring: standard products and image quality

Wouter Dierckx^{a*}, Sindy Sterckx^a, Iskander Benhadj^a, Stefan Livens^a, Geert Duhoux^a,
Tanja Van Achteren^a, Michael Francois^b, Karim Mellab^b, and Gilbert Saint^b

^aFlemish Institute for Technological Research (VITO) – Remote Sensing Unit, Boeretang 200, 2400 Mol, Belgium; ^bESA-ESTEC, Noordwijk, The Netherlands

(Received 31 August 2012; accepted 8 March 2013)

PROBA-V is a new global vegetation monitoring mission, to be launched in the second quarter of 2013. PROBA-V has been developed to show a consistent performance with SPOT-VEGETATION (SPOT-VGT) data, with similar spectral bands but with an improved spatial resolution of 1/3 km. The innovative mission concept has led to several key research topics related to image quality, which are discussed in this article. To support the existing VEGETATION user community, the data products for PROBA-V continue to provide daily top of canopy synthesis (S1-TOC) and 10 day synthesis products (S10-TOC). In addition, the new top of atmosphere daily synthesis (S1-TOA) products and a radiometrically/geometrically corrected (level 1C) product in raw resolution will also be provided for scientific users.

1. Introduction

Following 15 years of successful operations of VEGETATION 1 and 2 on, respectively, Système Pour l'Observation de la Terre (SPOT) 4 and 5 satellites, ESA has developed a Belgian-led Earth observation mission dedicated to global vegetation and land-cover monitoring (Schyns 2010). PROBA-V will be launched in early 2013 and is a continuation of the PROBA autonomous small satellite series (Bermyn and Dorn 2008). The two previous satellites in the series were demonstration missions providing an early flight to new technologies. Their relevance for users was only picked up later, with PROBA-1 for hyperspectral environmental monitoring and PROBA-2 for solar observations and space weather. PROBA-V however is from the start both an implementation of new technology and an operational mission, to ensure timely service of data towards the existing VEGETATION user community.

PROBA-V has an optical instrument on board that will provide 1 km and 1/3 km data products consistent with the familiar 1 km data products of SPOT-VEGETATION (Maisongrande, Duchemin, and Dedieu 2004). To achieve this, PROBA-V specifications align closely with those of SPOT-VEGETATION, while improving the spatial resolution on a smaller satellite. The new global mission concept is presented in this article, as well as specific topics related to data quality.

Once PROBA-V is launched, data will be calibrated and validated after a full commissioning of the satellite and the ground segment processing system is performed. Special focus is given to calibration, which is carried out through a consistent plan of

*Corresponding author. Email: wouter.dierckx@vito.be

Gilbert Saint is deceased and is included as co-author for important contributions made to Sections 3.2 and 3.6 of this article. We refer to the acknowledgements found herein.

vicarious calibration, on dedicated sites for radiometry (Sterckx et al. 2011; Sterckx, Livens, and Adriaensen 2013) and using ground control points (GCPs) chipmatching for geometry (Mica et al. 2012; Sterckx et al. 2013 this volume).

To support the existing VEGETATION user community, the data products for PROBA-V continue to provide S1-TOC and S10-TOC. In addition, the new S1-TOA and radiometrically/geometrically corrected data (level 1C) products in raw resolution (100 m for centre 500 km swath for the VNIR bands) are foreseen for scientific users.

These products are provided on a Web portal. An additional interface is developed, directed towards the user community of GMES, the programme for Global Monitoring for Environment and Security (Aschbacher 2012). Through its GMES Space Component Data Access Service (GSCDA), access to the PROBA-V 1 km synthesis products is provided by ESA.

2. The global mission concept

The prime application target for PROBA-V is continuous monitoring of land cover on a continental scale. This drives the mission requirements of global coverage, a near-daily revisit frequency, and a moderate spatial resolution. Similar to SPOT-VEGETATION, PROBA-V records data in four bands of a moderate spectral and high radiometric resolution. The PROBA-V satellite will follow a Sun-synchronous orbit at a height of 820 km, achieving a daily global coverage, besides the equatorial region (within 35° of the equator) where coverage is guaranteed every two days (Table 1).

The PROBA-V platform is the next satellite in the successful PROBA series, designed to perform its normal operations with minimal need for ground commanding. Ground station interaction is required only for pass scheduling and for uploading user requests (e.g. for calibration campaigns). New additions to the system are the X-band transmitter and flash-based mass memory (Vrancken et al. 2012). These allow it to fulfil its requirements within the constraints of power, volume, and mass. An additional constraint is imposed by the data volume, which can be downlinked for the memory budget; therefore, data is compressed on board using compression software made according to the Consultative Committee for Space Data Systems (CCSDS) standard. This standard differs from the well-known JPEG2000 standard in that it is specifically tuned for high-rate instruments used on board the spacecraft (CCSDS Secretariat 2005).

The payload consists of three cameras placed next to each other to achieve the swath necessary for global coverage. Each camera has two focal planes, one for the short wave infrared (SWIR) band and one for the visible and near-infrared (VNIR) bands (Versluys et al. 2012). The VNIR focal plane is used to capture a 'Blue' band, a 'Red' band, and an NIR band. The SWIR focal plane only captures one SWIR band, and covers the same swath as the VNIR plane. To cover the full focal plane for the SWIR band, three staggered detectors of 1024 pixels are used per camera, with an overlap area between each pair of detectors. This instrument layout is schematically represented in Figure 1.

Spatial resolution is the main performance improvement of PROBA-V compared to SPOT-VEGETATION. PROBA-V products will be delivered at two resolutions: the 1 km-resolution products known from SPOT-VEGETATION and the improved 1/3 km-resolution products. In addition, an alternative option is presented in a scientific level 1C product, which consists of radiometrically/geometrically corrected data in raw resolution. The spatial resolution of this product varies from 100 m × 100 m to 350 m × 160 m for the VNIR bands, and from 180 m × 185 m to 660 m × 300 m for the SWIR bands. The raw data resolution is best at near-nadir viewing (central camera, about 500 km swath),

Table 1. Platform and orbit specifications.

Platform	
Altitude	820 km
Local time of descending node	10.30–11.30
Inclination	Sun-synchronous orbit + 0.13°
Coverage	daily above 35° latitude; full coverage every 2 days
Payload Mass	33.3 kg
Payload dimensions	0.2 m × 0.8 m × 0.35 m
Power	43.2 W payload
Life	2.5–5 years
Data	16 Gb/pass
Downlink	11.1 Mb s ⁻¹ (after compression)

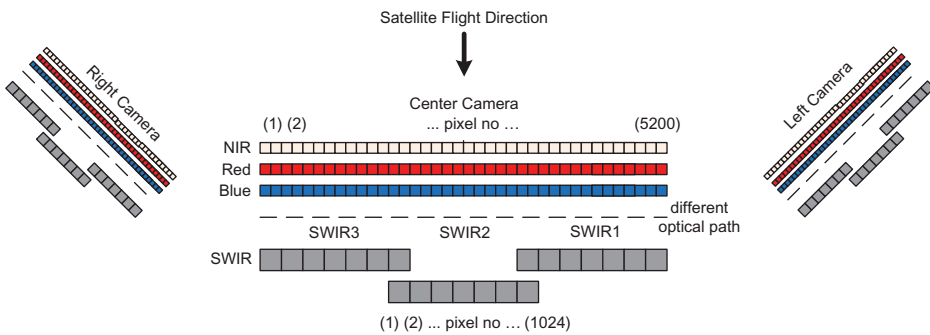


Figure 1. PROBA-V instrument design.

making this product interesting when spatial resolution is more important than the global coverage or a daily revisit frequency. More information on the products of the PROBA-V is provided in Section 4. The complete data processing chain is described elsewhere in this volume (Sterckx et al. 2014 this issue).

Radiometric and geometric specifications are provided in Tables 2 and 3. They are specified as mandatory for the 1 km product and as design goal for the 1/3 km product –

Table 2. Radiometric specifications.

Radiometric specifications		
Band centre (nm)	Bandwidth (nm)	SNR at L_{ref}
463	46	155 at 111 W m ⁻² sr ⁻¹ μm ⁻¹
655	79	430 at 110 W m ⁻² sr ⁻¹ μm ⁻¹
845	144	529 at 106 W m ⁻² sr ⁻¹ μm ⁻¹
1600	73	380 at 20 W m ⁻² sr ⁻¹ μm ⁻¹
Radiometric performance		
Absolute accuracy		5%
Inter-channel accuracy		3%
Stability		3%
Spectral misregistration		0.9 nm VNIR, 2 nm SWIR
Polarization sensitivity		4% for the Blue band; 1% otherwise

Table 3. Geometric specifications; HR denotes the 1/3 km product.

Geometric specifications	
Field-of-view and swath	102.4° and 2295 km
Ground sampling distance (GSD)	1/3 km × 1/3 km HR, 1 km × 1 km LR
Modulation transfer frequency (MTF)	> 30% at Nyquist frequency
Absolute geo-location accuracy	<1 HR GSD
Inter-band geo-location accuracy	<1/3 HR GSD
Multi-temporal geo-location accuracy	< 1/2 HR GSD

owing to the higher spatial resolution, specifications such as radiometric accuracy, signal-to-noise ratio (SNR at reference radiance L_{ref}), and geo-location accuracy become more challenging for a 1/3 km product than for a 1 km product. Users of SPOT-VEGETATION will see that the expected performance of the 1/3 km products is on par with that of 1 km SPOT-VEGETATION products. For the 1 km product, the specifications are less challenging and thus comfortably met.

For radiometric accuracy, a validation of PROBA-V's in-flight radiometric calibration methods using SPOT-VEGETATION provides a first indication that the involved specifications can be achieved in flight. Because PROBA-V's payload consists of three identical camera systems, a camera-to-camera calibration algorithm is used, which allows one to control the relative radiometric calibration of the three cameras (Sterckx, Livens, and Adriaensen 2013).

For geo-location accuracy, the on-ground prediction of the geo-location performances (based on a worst-case analysis of the platform and instrument stability) has demonstrated full compliance to the 1 km product, whereas for the 1/3 km product the multi-temporal geo-location accuracy is still to be demonstrated in flight (Table 3; Figure 2). The multi-

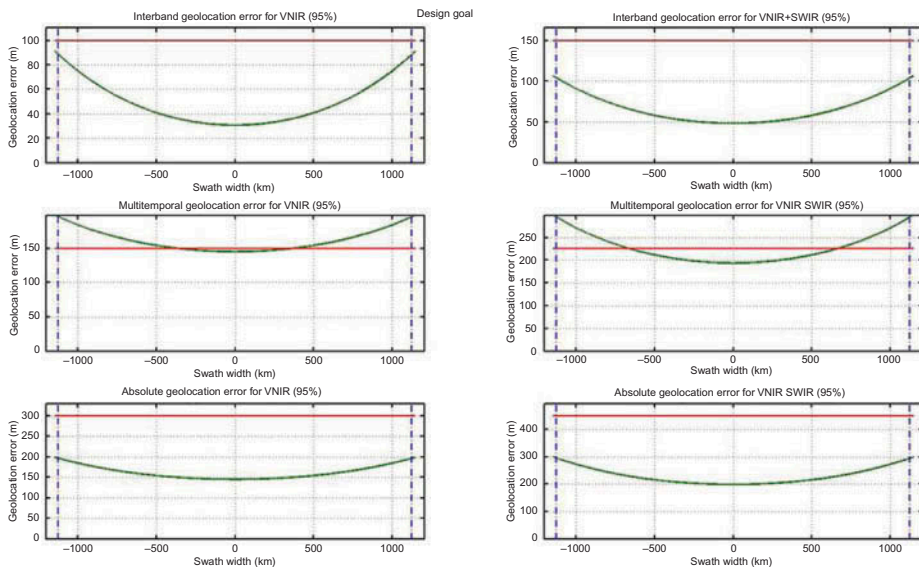


Figure 2. Predicted (green) 1/3 km geo-location performances of VNIR and SWIR bands based on a worst-case analysis of platform and instrument stability. Red line marks the 1/3 km (design goal) requirement. Blue lines mark the swath requirement.

temporal geo-location is affected by the positioning stability of the PROBA-V system over time, and hence to orbital and seasonal variations. To achieve this specification in flight requires a continuous geometric calibration system, which is carried out for PROBA-V using the GCP chip-matching method and by determining the geometric sensor model (Mica et al. 2012; Sterckx et al. 2014 this issue).

3. Topics of data quality

The new system concept of PROBA-V has resulted in several changes compared to the SPOT-VEGETATION mission. Specific software solutions have been developed to address these changes. A summary of the important changes to the PROBA-V mission concept is listed in Table 4, along with the developments carried out to ensure an optimal and consistent quality of the data. These are each discussed below.

3.1. Stretched bi-cubic mapping filter

Typically, to re-sample data from a variable spatial resolution lower than or equal to the fixed spatial resolution of the target product, a high-quality algorithm is the standard bi-cubic interpolation filter using four neighbouring grid points. This algorithm was used to remap SPOT-VEGETATION data. In PROBA-V however, as discussed above, the raw data resolution is much better than the product resolution and must therefore be downsampled.

Interpolation filters such as the standard bi-cubic interpolation filter are not fit to carry out downsampling: to derive a final value they only take the closest neighbouring points. In case of the standard bi-cubic interpolation filter, with the implementation used in SPOT-VEGETATION, the bi-cubic interpolation weight coefficients w_c are defined by

$$w_c(\mathbf{x}_c) = \begin{cases} (a+2)|\mathbf{x}_c|^3 - (a+3)|\mathbf{x}_c|^2 + 1, & \text{for } 0 \leq |\mathbf{x}_c| < 1 \\ a|\mathbf{x}_c|^3 - 5a|\mathbf{x}_c|^2 + 8a|\mathbf{x}_c| - 4a, & \text{for } 1 \leq |\mathbf{x}_c| < 2 \\ 0, & \text{for } 2 \leq |\mathbf{x}_c| \end{cases} \quad (1)$$

Table 4. Major changes and consequences compared to SPOT-VEGETATION mission.

Change compared to SPOT-VEGETATION	Consequence of the change
Variation of raw spatial resolution across the swath (100 m–330 m)	Stretched bi-cubic mapping filter used to achieve best-quality product resolutions (3.1)
Full data rate is too high to downlink with small satellite	Compression required to downlink the data (3.2)
Optimization of compression important for data quality	Optimization of data before compression using a dynamic integration time system (3.2)
No on-board calibration instrument	Vicarious calibration approach with strong investment in reliable multi-temporal calibration (3.3)
Three identical camera systems to cover swath instead of one	Camera-to-camera calibration algorithm used to control relative radiometric accuracy (3.3)
Geo-location budget necessitates in-flight geometric calibration	Continuous geometric calibration system using methodology of ground control points (3.4)
Temporal separation of bands by 12 s between first and last bands	Updated cloud detection algorithm accounting for cloud movement during 12 s (3.5)
Differences in spectral response	Evaluation of the spectral continuity with respect to SPOT-VEGETATION (3.6)

where x_c is the grid coefficient, the distance in grid coordinates as seen from the position where the filter is centred. In the SPOT-VEGETATION implementation, the parameter a is set to -0.5 . This setting is preferred to more negative values because it reduces undershoots and overshoots at land–sea borders (Figure 3).

It is clear from the above figure that standard bi-cubic interpolation offers no solution for downsampling, since it is not possible to assign positive weights to more than two pixels away from the centre location. Several downsampling filter options have therefore been investigated.

In **Option 1**, the ‘trapezium’ only option, instead of bi-cubic interpolation, a trapezium filter is used. As in the standard mapping algorithm, first an inverse model is applied to determine for an (x, y) position in the product grid the corresponding position in the raw image data (which has a ‘pixel-line’ or sensor grid). The pixel value is then determined by applying the trapezium filter on the raw image data with its centre at the determined (pixel-line) position. The trapezium filter (Figure 4) averages the raw image values over a

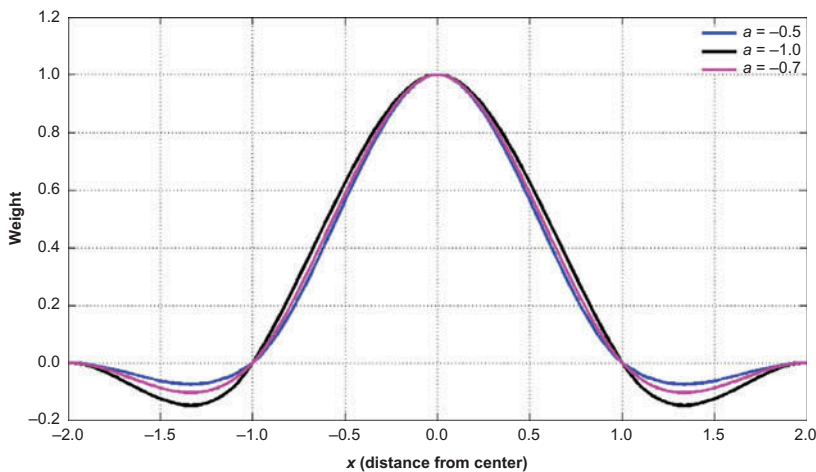


Figure 3. Bi-cubic filter implementations for different values of a .

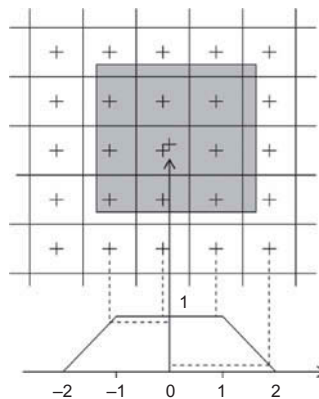


Figure 4. Trapezium filter, for a product pixel size = 3 times raw pixel size. X-axis: grid coefficient. Y-axis: filter weight coefficient.

length measured in pixels equal to the product resolution (this length is derived from the raw pixel resolution for the pixels involved, e.g. 100 m \times 100 m for near-nadir VNIR pixels). The resulting values are thus downsampled, and are then assigned to (x, y) positions in the product grid.

Option 2, the ‘trapezium-bicubic’ option, uses a strategy that allows applying low-pass filtering on the raw image data as a preprocessing step. As a result, interpolation filters can still be used in the mapping algorithm. It applies first the trapezium filter to the entire raw image (effectively smoothing the values of the image). Then, as in the previous option, the inverse model is applied from the product grid into the raw but smoothed image. The resulting pixel value is then determined by applying the bi-cubic interpolation filter on the pre-filtered image data and assigning the resulting values to (x, y) positions in the product grid.

A downside exists for both these options, however, owing to the use of the trapezium filter for low-pass filtering of the data. High spatial frequencies are not well-attenuated by such a filter, thus leading to aliasing effects (e.g. Moiré patterns when high spatial frequencies are present in the image).

Option 3, the ‘gauss-bicubic’ option, solves the aliasing issue by replacing the low-pass filtering filter of the ‘trapezium-bicubic’ by a Gaussian filter. This filter can suppress high spatial frequencies well. An unfortunate consequence is however that a Gaussian filter also reduces contrast for lower spatial frequencies, thereby reducing the contrast in the final product.

Option 4, the ‘stretched-bicubic’ option, which is the chosen algorithm for PROBA-V, consists of an adjustment to the standard bi-cubic interpolation filter, such that it is able to perform low-pass filtering and downsampling combined. This adjustment, termed the stretch factor, adapts the filter by stretching its extent according to the downsampling rate. As a result, no additional pre-filter is required.

The stretch factor is defined as

$$f_s = \begin{cases} \frac{\text{resolution}}{\text{pixelSize}} & \text{if } \frac{\text{resolution}}{\text{pixelStep}} > 1 \\ 1 & \text{if } \frac{\text{resolution}}{\text{pixelSize}} < 1 \end{cases} \quad (2)$$

where *resolution* is defined as the product pixel size (1/3 km or 1 km) and *pixelSize* is the pixel size in the raw data product. The grid coefficients x_s are then rescaled with the stretch factor f_s to obtain grid coefficients x_c , which can be inserted in the standard bi-cubic implementation (Equation (1)), i.e. $x_c = x_s/f_s$. Likewise, the final weight w_s is defined as $w_s = w_c/f_s$, which ensures the sum of the weights is equal to 1 (Figure 5).

A consequence of this stretch factor is that the dimensions of the stretched filter become larger. For example, for a 1/3 km product pixel remapped from data in the central camera, a convolution filter of 12 pixels \times 12 pixels at 100 m \times 100 m is used. At the edge of the swath at 350 m raw resolution across-track, the algorithm falls back to the classic bi-cubic interpolation with four weights.

Using the parameter $a = -0.5$ as is done for SPOT-VEGETATION, the bi-cubic interpolation filter implementation is almost identical to the Lanczos2 filter, defined as

$$\text{Lanczos2}(x) = \begin{cases} \frac{\sin(\pi x)}{\pi x} \frac{\sin(\frac{\pi x}{2})}{\frac{\pi x}{2}}, & \text{for } |x| < 2 \\ 0, & \text{for } 2 \leq |x| \end{cases} \quad (3)$$

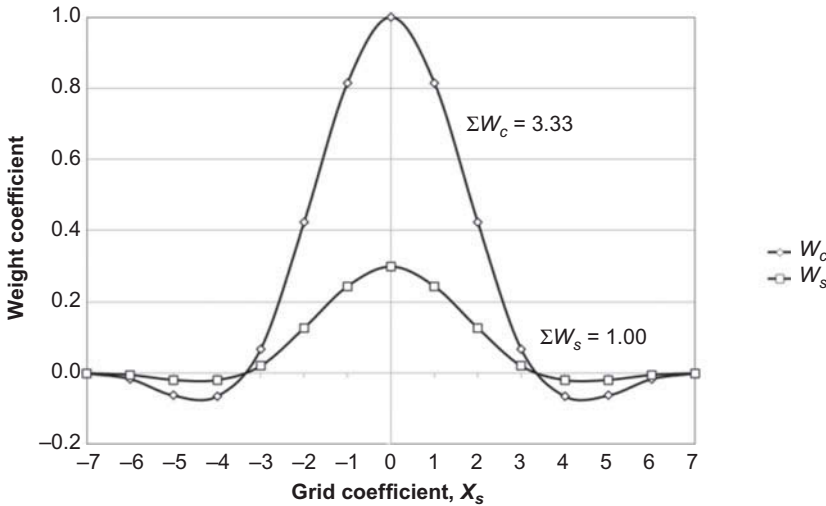


Figure 5. Stretched bi-cubic weights ($f_s = 3.33$, $a = -0.5$). Weight sums show need for scaling.

The Lanczos filters are considered the best filters for the combination of low-pass filtering and re-sampling (Turkowski 1990). The stretched bi-cubic interpolation filter offers a good trade-off between computational efficiency and the optimal image quality of the Lanczos2 filter. Still, as a convolution filter of $12 \text{ pixels} \times 12 \text{ pixels}$ in the central camera, the increase in computational complexity compared to the standard 4×4 bi-cubic interpolation filter should be noted. The mapping is therefore one of the most computation-intensive modules in the processing chain.

Further support for the assessment of the four discussed options can be gathered from the modulation transfer function (MTF) comparisons shown in Figure 6 below. MTF curves are plotted for a downsampling fraction of 3, corresponding to the $1/3 \text{ km}$ product. One set of curves is plotted for a phase of 0 (indicating that the filter centre coincides with the centre of a pixel). The second set of curves is plotted for a phase of 0.5 (indicating that

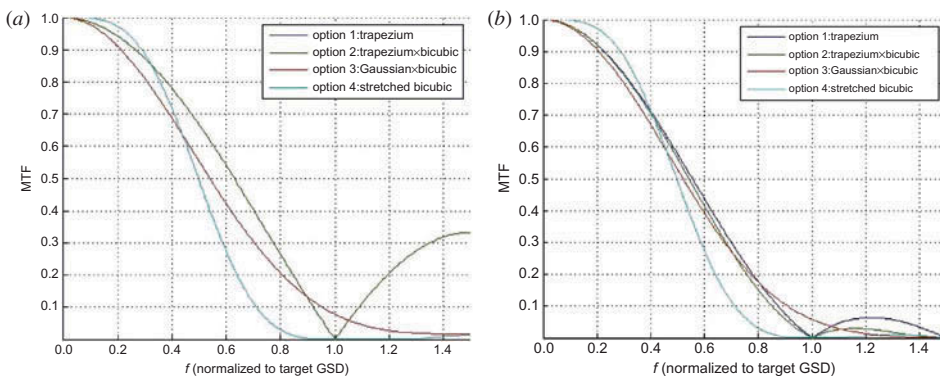


Figure 6. MTF comparison between four options for re-sampling implementation. Option 1 and Option 2 are identical for the phase 0 case. (a) All options downsampling $1/3$ and phase 0. (b) All options downsampling $1/3$ and phase 0.5.

the filter centre coincides with the edge between two pixels). In practice, the phase will vary uniformly between 0 and 0.5. Ideally the MTF of low-pass filtering is maximized for spatial frequencies below the Nyquist frequency 0.5, retaining the quality of the spatial frequencies in the target resolution, and rapidly falls to 0 beyond the Nyquist frequency 0.5 to attenuate the higher frequencies and aliasing effects.

For Options 1 and 2, the aliasing effect caused by the trapezium filter is clearly visible, as higher spatial frequencies are hardly suppressed (frequencies above the Nyquist frequency of 0.5 Ground Sampling Distance (GSD)). The Gaussian filter in Option 3 strongly improves the aliasing as expected. However, and especially for a phase of 0, the Gaussian filter also reduces contrast for spatial frequencies below Nyquist.

The main advantages of the stretched bi-cubic over these options are that it provides the best trade-off between contrast reduction and anti-aliasing and that it adapts itself to the downsampling rate over the FOV using the stretch factor, thereby avoiding the need for a smoothening filter. In addition, there is no variation in MTF effect over different phases. It is thus better for image quality than the combination of the standard bi-cubic filter and an additional filter for low-pass filtering. The added computational complexity compared to the standard bi-cubic filter must however be accounted for.

3.2. Data compression and dynamic integration time

Because the amount of raw data captured by the PROBA-V instrument is larger than the available downlink capacity, the satellite has been equipped with an on-board data compression unit. The data volume is reduced through image compression according to the CCSDS standard (Fiethe et al. 2007; Michalik et al. 2006). This compression is not lossless but introduces noise in the data, which has a non-negligible impact on the SNR (Livens and Kleihorst 2009). The impact has been assessed in this study by examining RMSE values caused by compression on 30 representative 12-bit images, 10 for each VNIR spectral band (Blue, Red, and NIR). The images were based on MERIS 300 m full resolution data, with its digital number (DN) values rescaled to function as simulated PROBA-V 300 m products. Simulated PROBA-V 1 km products were obtained by upsampling as described in the study. The study examined the effect of compression for 300 m products instead of 1/3 km products, and also for 1 km products. The RMSE values show that the 1 km product is affected less. This can be explained by the fact that compression noise is reduced by averaging over the neighbouring pixels. Moreover, the lossy CCSDS compression scheme introduces noise predominantly at higher spatial frequencies, which is reduced the most by the spatial averaging. The compression ratios (CR) used in the study are shown in Table 5. Table 5 also compares the RMSE values obtained in the study for the 1 km product, with a prediction based on the RMSE values obtained for the 300 m product, using the following relation:

$$\text{RMSE 1 km} = \frac{300 \text{ m}}{1 \text{ km}} \text{RMSE 300 m} \quad (4)$$

This relation describes the reduction of noise due to spatial averaging. The RMSE of compression noise is reduced by the square root of the amount of samples used for averaging. For square product pixels, this amount is defined by the ratio of the resolution of the two products.

Table 5. Root-mean square error (RMSE) analysis on simulated PROBA-V products, showing improvement of RMSE for lower-resolution products. ('CR' = 'compression ratio'; 'DN' = 'digital number').

Band	CR	DN RMSE (300 m)	DN RMSE (1 km)	Spatial resolution (1 km/300 m)	DN RMSE (1 km prediction)
Blue (centre)	10.8	0.67	0.28	3.33	0.20
Red (centre)	7.2	1.68	0.56	3.33	0.50
NIR (centre)	5.4	2.97	1.03	3.33	0.89
Blue (side)	10.8	1	0.38	3.33	0.30
Red (side)	7.2	2.92	0.86	3.33	0.88
NIR (side)	5.4	4.86	1.56	3.33	1.46

It can be seen that the predicted RMSE reduction is slightly larger than the observed reduction, but matches the general trend quite well. The RMSE values are reduced by about a factor 3.3 in the 1 km product, compared to the 300 m product.

The data rate budget constraint of the PROBA-V system requires an average compression ratio of 3.5. The compression ratios are however tuned for each camera and band for the following three reasons.

- Compression noise in a lossy compression mode can be reduced by averaging over neighbouring pixels as is carried out in the mapping filter of Section 3.1 (Livens and Kleihorst 2009). For the centre camera, initial pixel sampling is about 100 m in the across-track direction, whereas it is larger for the side cameras. Therefore, more averaging can take place, errors will be more reduced, and thus higher compression ratios can be chosen for the centre camera.
- The compression ratios for the Blue band were set to a high value compared to the other bands. Results show that the Blue band has low RMSE values even when using high compression ratios (Livens and Kleihorst 2009). This is because the Blue band tends to contain fewer high spatial resolution features and has a smaller dynamic range compared with the other bands in PROBA-V-type remote-sensing data.
- The compression ratios for the SWIR band are currently chosen to be near-lossless. The SWIR band is imaged at a lower spatial resolution, and therefore it accounts for only a small portion (less than 9%) of the total amount of raw data. Increasing the compression ratio of the SWIR band will thus allow only a small reduction of the compression ratio for another band. Moreover, owing to the lower spatial resolution, compression noise for the SWIR would not be reduced as much by the mapping filter, and so it is proposed to minimize the noise for the SWIR.

The currently defined compression ratios are indicated in Table 6.

The dynamic range of the image has an impact on compression. When the dynamic range of the sensors is optimally used generating high signals in different illumination conditions, compression, which typically affects only the least significant bits of the signal, leaves most of the signal intact and thus has a relatively low impact. This can be achieved by setting high exposure (i.e. high integration time), such that the brightest input signal coincides with the maximum signal of the sensor's useful range. However, the reflectance received by the sensors varies considerably because the Sun illumination

Table 6. Compression factors for an average compression of 3.5.

Band	CR
Blue (centre)	11.0
Blue (side)	4.9
Red (centre)	4.7
Red (side)	2.9
NIR (centre)	4.0
NIR (side)	2.7
SWIR (centre)	2.4
SWIR (side)	1.8

(expressed as Sun zenith angle (SZA)) changes over the seasons and during each orbit. In the PROBA-V system, this effect is optimized by adapting the exposure (integration time) over the orbit.

A detailed study has been performed to calculate the darkest and brightest land-cover signal in radiance (L_1' and L_3') as a function of SZA, during an orbit and over the seasons. The radiance levels L_1' and L_3' define the minimum and maximum radiance levels for land-cover sites in varying illumination conditions over the year and exclude radiance levels for calibration targets such as oceans. The latter are excluded, since in calibration mode images will typically be acquired uncompressed and instrument parameters (integration time, gain, line period) are set specifically for the specific target characteristics and illumination conditions. The study uses a dataset of representative reflectance spectra for land cover, different types of vegetation, and soil (Figure 7), which shows that the virtual radiance levels L_1' and L_3' function as a good envelope for these spectra. It is crucial to distinguish L_1' and L_3' from the specification of minimum and maximum radiance levels (L_1 and L_3) for the overall mission, which also includes, e.g., water radiances. The virtual radiances L_1' and L_3' are only used to model the

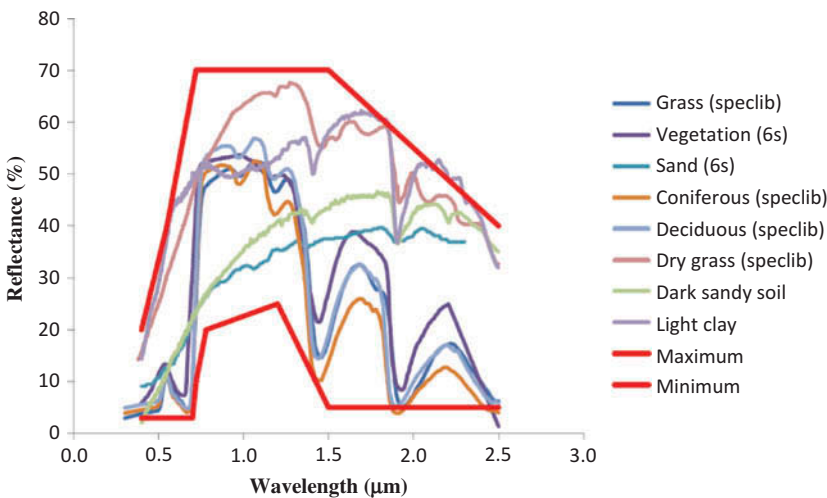


Figure 7. Typical land-cover spectral reflectances and upper/lower envelopes.

Table 7. Reference radiance levels for PROBA-V ($\text{W m}^{-2} \text{sr}^{-1} \mu\text{m}^{-1}$).

	L_1	$L_2 = L_{\text{ref}}$	L_3	$L_4 = L_{\text{max}}$
Blue	39	111	236	567
Red	10	110	231	446
NIR	4	106	212	296
SWIR	0.6	20	38	58

radiance variation of land cover over latitudes, whereas L_1 and L_3 are used to define the optimal signal range of the instrument (and are defined by setting L_3 close to 90% of the full range, and evaluating that L_1 can be observed with sufficient accuracy). The reference radiance levels are provided in Table 7 for comparison, also including L_2 (the radiance level for SNR calculation) and L_4 (the maximum radiance to be observed by the instrument).

The Sun-satellite geometry uses a simplified circular orbit model with a constant precession rate enabling Sun-synchronicity. This is sufficient to simulate the 820 km orbit with sufficient accuracy.

Sun-satellite observation angles (zenith and azimuth angles) are simulated with an angular resolution of 0.7° . An orbit calculation is used to compute the geographical position (latitude/longitude), satellite position (zenith and azimuth angles), and Sun position (zenith and azimuth angles). Sun positions were computed for two extremes of local solar time of the descending node (10:30 and 11:30), and for each month on the 21st day. Nominal atmospheric conditions were chosen and applied using the 6s model (Kotchenova et al., 2006) with a mid-latitude summer model (water vapour = 2.93 g cm^{-2} , ozone = $0.319 \text{ cm-atmospheres}$ or 0.142 mol/m^2 of ozone), continental aerosol, visibility 23 km (defined as aerosol optical thickness of 0.23 at 550 nm). Pixel altitude is set at sea level.

By inserting these characteristics, together with the spectral responses of PROBA-V, into a 6s model, radiances can be computed for each relevant case. The important Sun zenith angle variation is shown for one orbit in Figure 8, along with the calculated radiance levels for that orbit. It clearly shows the strong correlation of L_1' and especially L_3' with the Sun zenith angle variation.

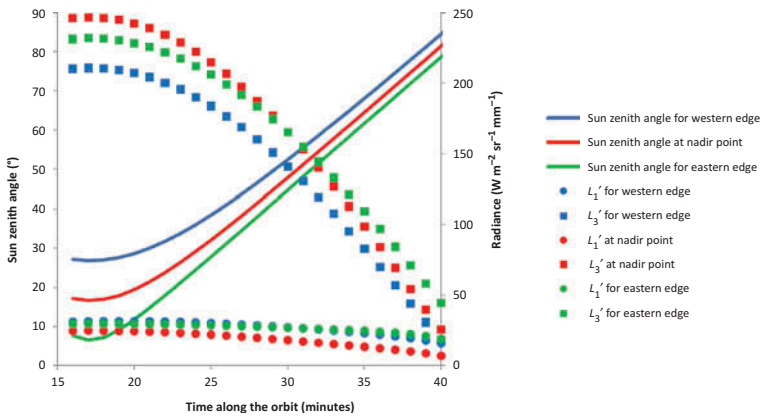
Figure 8. Sun zenith angle variation and radiance L_1' – L_3' over the daylight part of an orbit.

Table 8. Radiance values for the Sun zenith angle variation model ($\text{W m}^{-2} \text{sr}^{-1} \mu\text{m}^{-1}$).

Spectral band	L_1' (lower envelope)		L_3' (upper envelope)	
	a_1^n	b_1^n	a_3^n	b_3^n
Blue	40	20	150	60
Red	22	3	280	0
NIR	50	0	217	1
SWIR	2.8	0.2	48	1

The simplest way to model the minimum and maximum radiances (L_1' and L_3') as functions of the Sun zenith angle has been found to be with a cosine function of the following type:

$$L_i^n = a_i^n \cos z + b_i^n \quad (5)$$

where z is the Sun zenith angle of the sub-satellite point (centre of line) and L_i^n is the radiance to be modelled. a_i^n and b_i^n are coefficients, with n being 1–4 for the spectral bands 1–4 and i being 1 or 3 for L_1' and L_3' . Table 8 provides values for a_i^n and b_i^n .

These cosine relations are used to define an Integration Time Matrix (ITM) file, which defines the nominal integration time to be used for a given Sun zenith angle, in order to achieve maximum exposure of L_3' . The list of integration time steps is such that the change of integration time is gradual, and follows the variation of radiance close enough. Moreover, the change in integration time is taken into account in the sensor model of the data processing (Sterckx et al. 2014 this issue), which ensures the rescaling of data products for integration time.

The ITM file is uploaded to the PROBA-V on-board software (OBSW), which calculates the perceived Sun zenith angle of the satellite and determines the integration time to be used on board via the ITM file. In this way, optimal exposure can be achieved, which allows one to reduce RMSE errors induced by the compression.

The effect of compression was evaluated on simulated PROBA-V images, using ‘worst-case’ images, which are very difficult to compress (Figure 9), where image data digital numbers were scaled such that L_3 corresponds to 90% of a 12-bit dynamic range, which resembles the behaviour that can be expected from ITM. The RMSE values were determined for these images, and the maximum RMSE for the images is reported in Table 9 for raw resolution data. Also reported are the predicted RMSE reductions for the 1/3 km (=333.3 m) product and the 1 km product, and these are compared against the noise equivalent difference expressed as a digital number (NEDN), which is the requirement for the smallest radiometric difference the user wants to detect.

These results show that the RMSE effect for the side and centre cameras is balanced. The RMSE effect for the SWIR band is smaller, which is logical since we chose to have near-lossless compression for the SWIR. The most important conclusion is that the RMSE values are below the NEDN for the 1 km product for all bands, indicating that compression will not be an issue for this product. However, RMSE values for the 1/3 km product are up to 2 NEDN for the Red, NIR, and SWIR bands, and up to 3 NEDN for the Blue band. This shows that in the worst-case estimation here, compression noise will be noticeable as a small image difference in the 1/3 km product. A final estimation of the compression impact on image quality will be performed during commissioning and if required compression ratios and ITM can be updated accordingly.

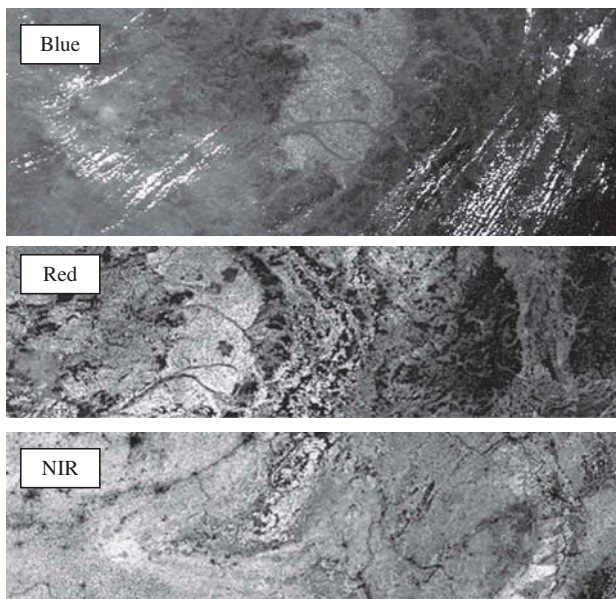


Figure 9. Worst-case PROBA-V simulated images for VNIR compression tests.

Table 9. Worst-case impact of compression comparing RMSE against NEDN.

Band	CR	Raw resolution (m)	RMSE (raw)	RMSE (333.3 m prediction)	RMSE (1 km prediction)	NEDN (12 bit)
Blue (centre)	11	96	35	10.1	3.4	4
Red (centre)	4.7	97	30	8.7	2.9	5
NIR (centre)	4.0	97	26	7.5	2.5	6
SWIR (centre)	2.4	183	9	2.5	1.6	7
Blue (side)	4.9	241	12	8.7	2.9	4
Red (side)	2.9	243	11	8.0	2.7	5
NIR (side)	2.7	244	10	7.3	2.4	6
SWIR (side)	1.8	454	4	2.7	1.8	7

3.3. Radiometric calibration

As the satellite has no on-board calibration facility, a vicarious calibration plan is used to monitor the sensor performance over time. This will include calibration over dedicated sites, which can be either nominal sites (made available also as products to users) such as deserts or non-nominal sites such as oceans or the moon. Several independent methods are used, results of which will be combined to reduce the uncertainty in the results, to provide validation, and to determine and to account for systematic errors in one or more techniques (Sterckx et al. 2013 this volume).

Many of the radiometric calibration methods used are based on prior calibrations defined for SPOT-VEGETATION (Vermote et al. 1992; Vermote and Kaufman 1995; Hagolle et al. 1999; Fournie et al. 2002; Hagolle et al. 2004; Fournie et al. 2007; summarized in Henry 2001). These have subsequently been implemented and validated

for PROBA-V, showing that the specifications of radiometric accuracy are achievable goals (Sterckx, Livens, and Adriaensen 2013).

Additional work has been carried out to develop a calibration method based on the use of top of atmosphere simulations over bright desert surfaces as an absolute reference. Validation of the approach using various satellite data (i.e. Aqua-MODIS (Moderate Resolution Imaging Spectroradiometer), MERIS (Medium Resolution Imaging Spectrometer), AATSR (Advanced Along Track Scanning Radiometer), PARASOL (Polarization and Anisotropy of Reflectances for Atmospheric Sciences coupled with Observations from a lidar), and SPOT-VGT extracted from the ESA Database for Imaging Multi-spectral Instruments and Tools for Radiometric Intercomparison (DIMITRI)) (<http://www.argans.co.uk/dimitri/>) has shown that absolute calibration over the Libya-4 desert is achievable with this approach with an accuracy of 3% (Govaerts, Sterckx, and Adriaensen 2013).

Multi-temporal calibration will be carried out on deserts, and is under investigation to be carried out also on the moon. The imaging of the moon will require an agile manoeuvre of the satellite based on preprogrammed attitude manoeuvres (Vrancken et al. 2012).

The three cameras of the PROBA-V payload are calibrated separately for all of the methods of the calibration described above, and will thus also have different operational calibration coefficients. To control and minimize inter-camera deviations, a camera-to-camera calibration method is used based on the overlap area between two adjacent cameras. The camera-to-camera calibration method can deliver a continuous check with respect to the temporal evolution of the radiometric calibration coefficients of the different cameras and allows detecting biases between cameras.

Finally, a statistical approach has been applied to combine the information from all methods into suitable operational calibration coefficients. The decision to update calibration coefficients is taken by the calibration manager based on these inputs. The complete description of the operational use of these methods is described elsewhere in this volume (Sterckx et al. 2013).

3.4. Geometric calibration

PROBA-V's three-mirror anastigmatic (TMA) imagers are designed to have all parts including the mirrors to be made from the same aluminium material (Versluys et al. 2012). Therefore, the imagers respond quasi-athermally and allow the platform to achieve its geo-location performances with only passive thermal control.

Still, thermo-elastic properties of the system can vary slowly, as demonstrated through extensive analysis with the thermo-elastic model (TEM) provided by ESA. This model shows that the main geometric behaviour of the system is a response to changes in the Sun's position and can be modelled by a slow deformation over the seasons, and a smaller periodic component over the latitudes, which is repeated in each orbit. Both these behaviours are carefully modelled by the geometric calibration system (Mica et al. 2012). Calibration parameters will be updated every four weeks and will track the response to the Sun's position by monitoring the Sun beta angle for seasonal effects, and the time out of eclipse for orbital effects (Sterckx et al. 2014 this issue).

The geometric calibration is based on GCP matching, using the global Landsat Geocover 2000 dataset as a reference (MDE Federal 2004). The calibration strategy consists in deriving calibration parameters for each scene selected for geometric calibration, which will have a scene size corresponding to the full swath per camera and an amount of lines equal to 800 km. Calibration parameters of multiple scenes will then be

combined through weighted constrained linear fitting to generate final calibration parameters. The final calibration parameters will then have a reduced error, owing to a weighted averaging effect, with respect to single-scene parameters.

3.5. Cloud detection algorithm

Similar to SPOT-VEGETATION, cloud detection is an essential part of the preprocessing chain for various added value products of the PROBA-V mission. The SPOT-VEGETATION algorithm for cloud detection is based on a simple threshold rule on the Blue and SWIR spectral bands (Lisens et al. 2000). In PROBA-V, however, the temporal separation between bands is up to 12 s (between NIR and SWIR), and the location of clouds in the SWIR image can be different from the location of clouds in the NIR and Blue bands, because of cloud movement (Figure 10). The movement caused by a difference in viewing directions between Blue and SWIR ($d_4 + d_3$ in Figure 10) combined with the shift due to wind speed will not exceed three pixels along-track and one pixel across-track (in both directions left and right).

Hence, the cloud algorithm for PROBA-V produces two masks for Blue and SWIR separately (Sterckx et al. 2013 this volume). A 3×3 search mask is applied to determine the matching SWIR pixel for the Blue band mask, and the matching Blue pixel for the SWIR band mask (Figure 11). The threshold rule for Blue and SWIR is then applied to each mask. To take into account the movement of the cloud between Blue and SWIR, a dilatation of one pixel is applied to the Blue mask (making the Blue mask effectively a VNIR mask). The VNIR and SWIR band masks are then merged by union to produce the final cloud mask.

The cloud detection algorithm has been analysed on five test images, where a reference mask was calculated assuming no temporal separation between bands, which was then compared with a mask using the actual separation for the PROBA-V system.

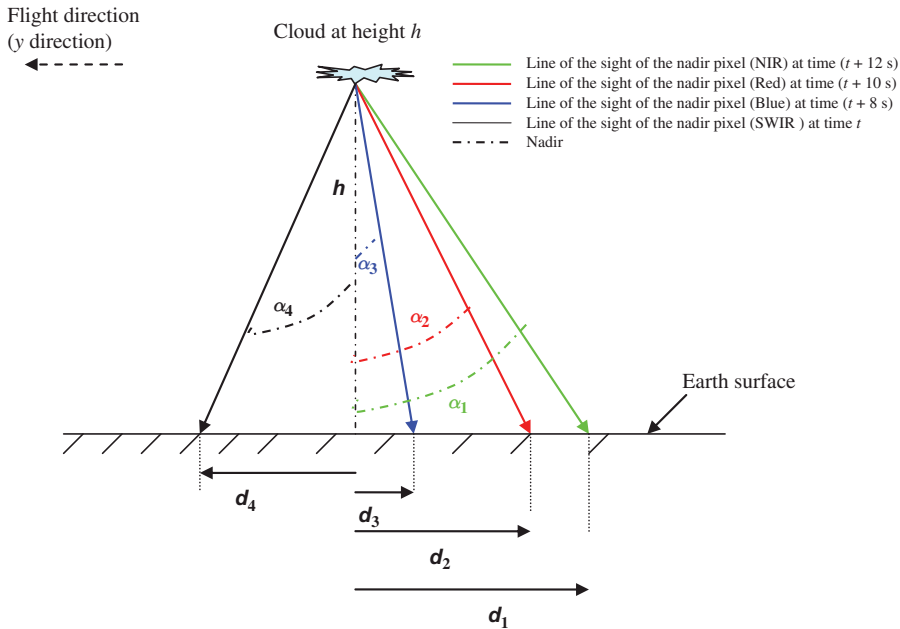


Figure 10. Schematic of cloud movement due to temporal separation.

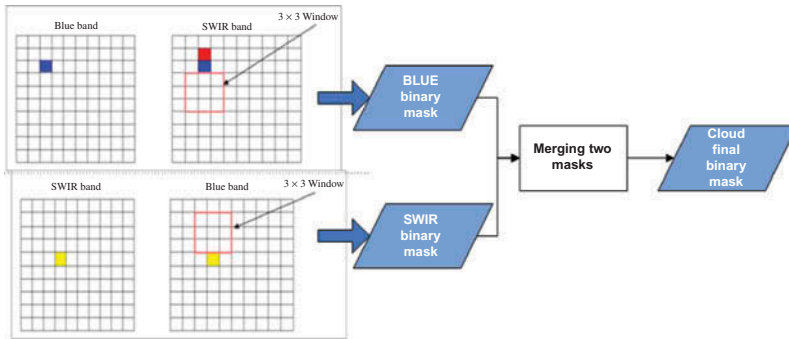


Figure 11. Cloud detection algorithm.

Another comparison was made between the reference mask and a dilatation of the reference mask by one pixel. This is considered a drastic alternative, but is used to compare the performance of the PROBA-V algorithm with respect to over-detection (amount of false positives). The results of this analysis are summarized by the following statistics for both PROBA-V algorithm and dilated mask (Table 10):

- overall accuracy (amount of correct classification);
- kappa statistics (Cohen’s kappa coefficient, sometimes proposed as the standard of classification accuracy; see Cohen 1968 and Smits, Dellepiane, and Schowengerdt 1999);
- percentage of cloud over-detection (amount of false positives);
- percentage of cloud under-detection (amount of false negatives).

Table 10 shows that the under-detection of clouds (false positives) is below 1% for the PROBA-V algorithm, and the over-detection (false negatives) is comparable to a dilatation mask of one pixel. The under-detection values for the dilated case are meaningless and therefore not used in the comparison. The size of clouds is the determining factor in the under-detection results: the highest error of 0.74% is found when many small clouds are present, whereas a smaller error of 0.14% is found when fewer and large clouds are present (Figure 12).

Table 10. Cloud algorithm comparison by statistics for five test cases.

Simulation	Overall accuracy (%)		Kappa coefficient		Cloud under-detection rate (%)	Cloud over-detection rate (%)	
	Predicted	Dilated	Predicted	Dilated	Predicted	Predicted	Dilated
Sim 1	93.50	91.20	0.84	0.79	0.38	25.06	34.33
Sim 2	93.98	93.04	0.85	0.83	0.14	8.84	10.37
Sim 3	78.12	74.94	0.55	0.48	0.48	41.28	47.76
Sim 4	85.95	83.50	0.66	0.61	0.51	64.82	76.62
Sim 5	76.26	71.41	0.53	0.43	0.74	48.60	59.07

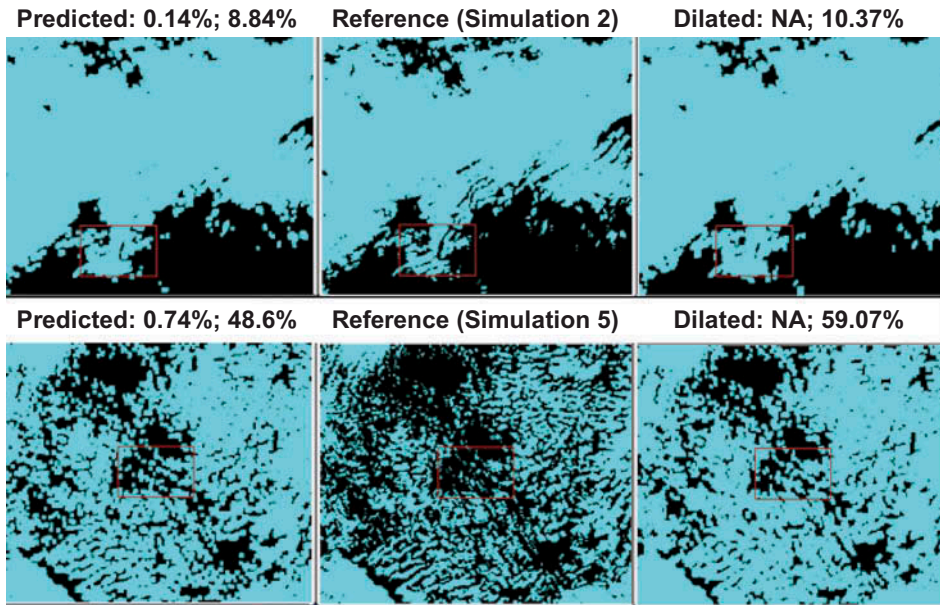


Figure 12. Cloud test cases (the rates of under-detection and over-detection are shown as percentages above each plot; NA = not applicable).

The situation presented in the results, with a fairly high value for over-detection and a low value for under-detection, is considered preferable. Although the effective coverage (i.e. the amount of pixels flagged ‘clear’) is reduced by over-detection, the radiometric quality close to clouds is typically suboptimal owing to cloud gradients. Furthermore, the cloud algorithm performs better than a standard dilatation of one pixel. A final optimization of the cloud algorithm will be performed during commissioning by fine-tuning the cloud threshold values.

3.6. Continuity of spectral response

Similarity between the spectral bands of PROBA-V and those of SPOT-VEGETATION is essential to allow continuity of long-term-derived products such as the normalized difference vegetation index (NDVI). A comparison of the spectral responses of PROBA-V with the SPOT-VEGETATION bands (Figure 13) clearly shows that a straightforward similarity between the two is not the case. Especially, the NIR band has a very asymmetric spectral response compared to the more Gaussian response curves of SPOT-VEGETATION 1 and 2 (VGT1 and VGT2).

A detailed investigation has been performed to determine the impact of these spectral response differences on both individual band reflectance and derived NDVI index. For a representative set of land covers ranging from bare soils to dense vegetation, the band reflectance is calculated as

$$\rho_{i,k} = \int_{\lambda_i^{\min}}^{\lambda_i^{\max}} R_i(\lambda) \rho_k(\lambda) E(\lambda) d\lambda / \int_{\lambda_i^{\min}}^{\lambda_i^{\max}} R_i(\lambda) E(\lambda) d\lambda \quad (6)$$

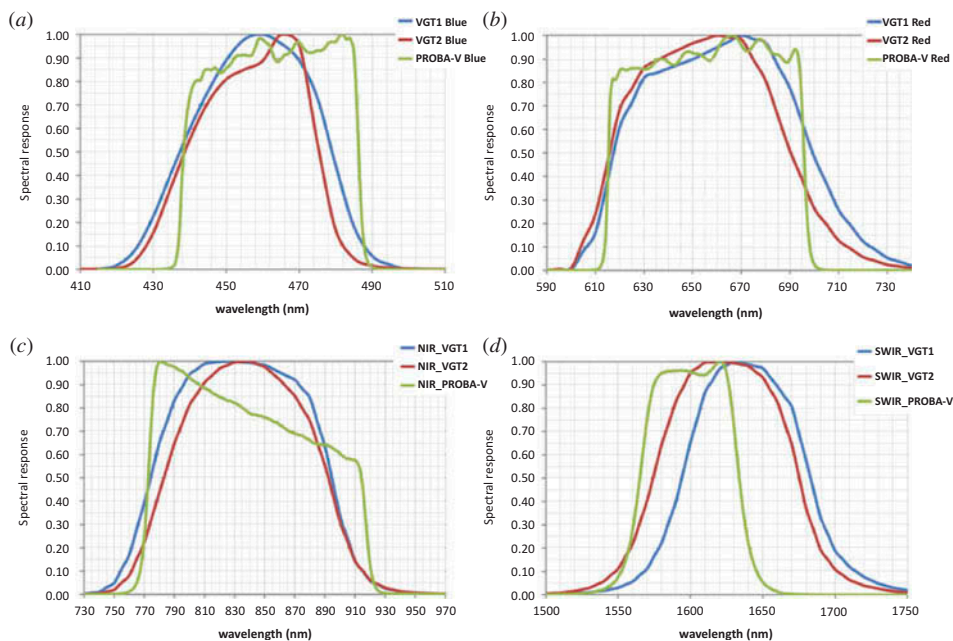


Figure 13. Comparison of spectral response curves for SPOT-VEGETATION 1 and 2, and PROBA-V. (a) Blue. (b) Red. (c) NIR. (d) SWIR.

where $\rho_{i,k}$ is the band reflectance for band i with land-cover type k ; $\lambda_i^{\min}, \lambda_i^{\max}$ are the minimum and maximum wavelengths of band i ; $E(\lambda)$ is the spectral irradiance; $\rho_k(\lambda)$ is the spectral reflectance of land-cover type k ; and R_i is the spectral response curve of the instrument for band i . Waterbodies, snow, and clouds were not included in the study because of their minor relevance for the mission.

Following Equation (7), the reflectances are computed for VGT1, VGT2 and PROBA-V bands. Based on the calculated band reflectances the NDVI is calculated as follows:

$$\text{NDVI} = (\rho_{\text{NIR}} - \rho_{\text{RED}}) / (\rho_{\text{NIR}} + \rho_{\text{RED}}) \quad (7)$$

Figure 14 and Table 11 compare VGT2 and PROBA-V against VGT1 as the reference. For the NIR and Red bands, differences between PROBA-V and VGT1 are of the same order of magnitude as those between VGT1 and VGT2. As a result, the NDVI differences are also quite similar. It is important to note as well that the NDVI contrast values are, compared to VGT1, higher for both PROBA-V and VGT2, which is considered advantageous for user applications on vegetation monitoring.

For the Blue band, the difference between PROBA-V and both VGT1 and VGT2 is larger, PROBA-V reflectances are higher, and particularly for higher reflectances (Figure 14). Still, the absolute reflectance difference is generally well below 0.003 (Figure 15), which is a user specification maintained from VGT as the noise equivalent reflectance difference to obtain a good aerosol estimation with the Blue band (Saint 1995).

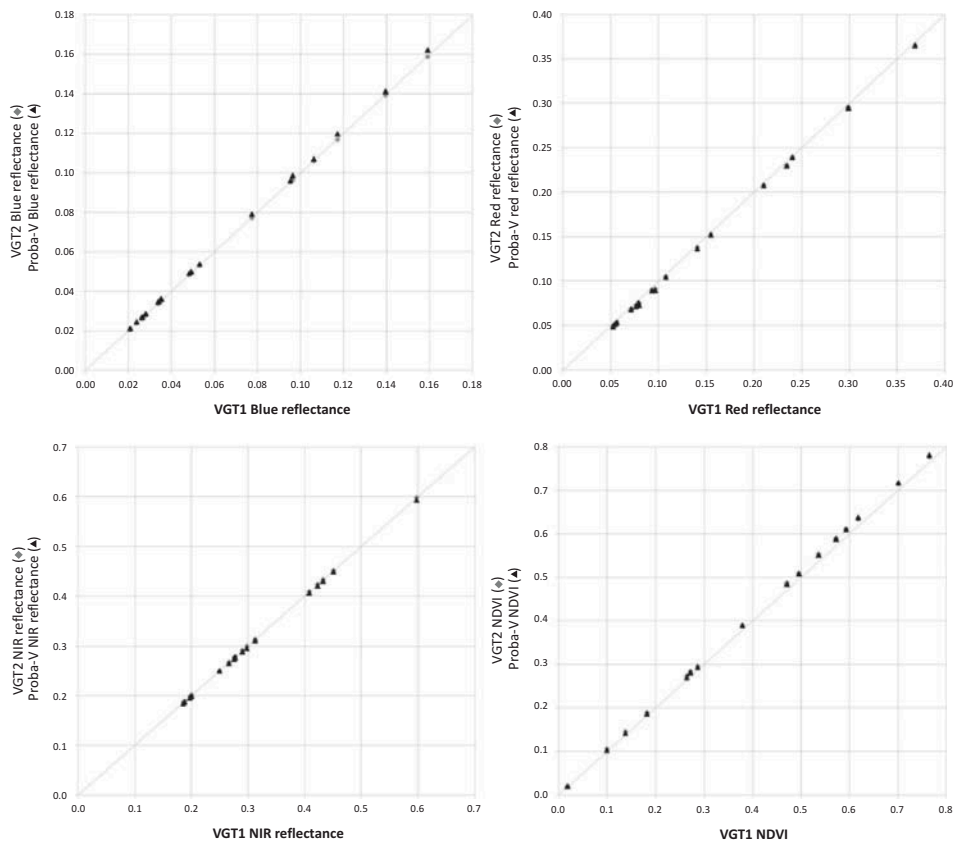


Figure 14. Plots of band reflectance and NDVI against VGT1 for the different cover types (grey line is 1:1 line).

Table 11. Average relative difference in band reflectance and NDVI.

	VGT2 minus VGT1	PROBA-V minus VGT1	PROBA-V minus VGT2
Blue reflectance difference (%)	-0.133	1.975	2.111
Red reflectance difference (%)	-3.214	-3.914	-0.735
NIR reflectance difference (%)	0.293	-0.471	-0.761
SWIR reflectance difference (%)	-1.373	-4.654	-3.366
NDVI difference (%)	3.676	3.335	-0.327

This specification defines the noise threshold, indicating that any reflectance difference smaller than this threshold is not considered significant.

Still, for long-term monitoring of a specific site, spectral response differences might be sufficiently significant for the application to take into account when moving from VGT1 or VGT2 image data to PROBA-V. For time-series analysis, the application of correction functions that account for the spectral response differences between sensors significantly

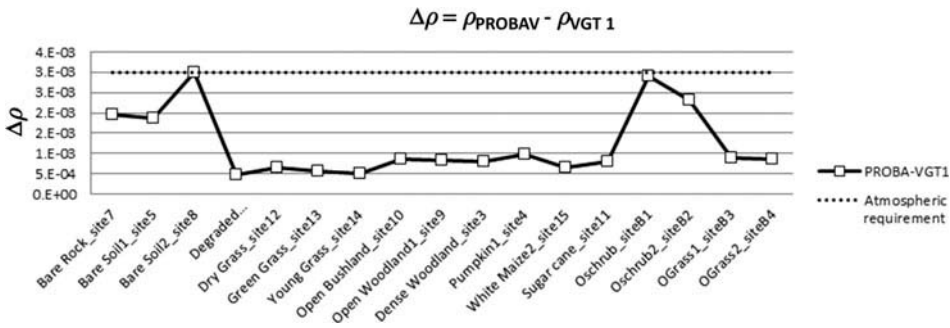


Figure 15. Plot of absolute difference in Blue band reflectance ($\Delta\rho$) between PROBA-V and VGT1 for different sites.

improves the consistency. This has been investigated for data from various National Oceanic and Atmospheric Administration (NOAA) missions, where relative reflectance differences compared to NOAA-9 ranged from -2% to 4% in the NIR, and from -25% to 12% for the Red band (Swinnen 2008; Trischenko 2009).

For the SWIR band, a similar investigation was performed on representative land-cover types to examine the consequence of the wavelength shift to lower wavelengths. Instead of the NDVI, the Normalized Difference Water Index (NDWI) is calculated:

$$\text{NDWI} = (\rho_{\text{NIR}} - \rho_{\text{SWIR}}) / (\rho_{\text{NIR}} + \rho_{\text{SWIR}}) \tag{8}$$

In Figure 16 the comparison for band reflectance and NDWI is made of PROBA-V and VGT2 against VGT1 as the reference. The PROBA-V SWIR reflectance values are on average 4.65% and 3.4% lower compared to VGT1 and VGT2, respectively.

More importantly, the position of the PROBA-V bands improves the discrimination of land-cover types based on NDVI and NDWI. The regression of PROBA-V NDWI against VGT1 NDWI shows a slope steeper than the 1:1 line, which indicates a better resolving power for the PROBA-V NDWI values (Figure 16).

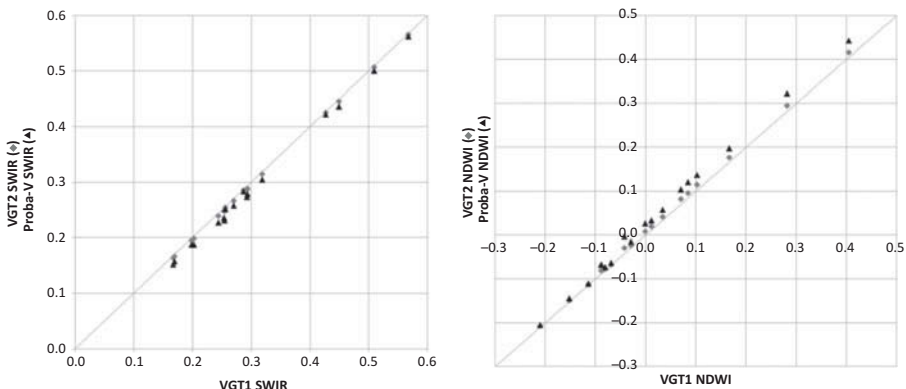


Figure 16. Comparison of SWIR (left) band reflectance and (right) NDWI for SPOT-VEGETATION 2 (VGT2) and PROBA-V with respect to SPOT-VEGETATION 1 (VGT1)

4. Data products

The products of PROBA-V are very similar to the standard VEGETATION products from SPOT-VEGETATION 1 and 2, to ensure data continuity towards the user community.

With its collection of standard products, PROBA-V continues to provide S1-TOC and S10-TOC products. These contain ground reflectance values, with best-quality and cloud-free data selected for the composite time period. In addition, users can request S1-TOA products – top of atmosphere daily synthesis products – containing values with no atmospheric correction applied. All synthesis products are available at two spatial resolutions: a lower resolution of 1 km as in VEGETATION products and a higher resolution of 1/3 km.

A fourth standard product is the radiometrically/geometrically corrected data (level 1C) product in raw resolution, adapted for scientific applications requiring highly accurate physical measurements. Compared to the S1-TOA product, it is not projected (mapping) and no shadow detection, cloud, or ice/snow detection is applied. Custom algorithms for these steps and for atmospheric correction can therefore be applied to these products. An overview of the standard products, containing a description of the main data layers, is provided in Table 12. The processing chain for these products is discussed in more detail elsewhere in this issue (Sterckx et al. 2014).

The standard products can be accessed by the user using a VITO Web portal (discussed in Sterckx et al. 2014 this issue). In addition to the VITO Web portal, an interface to ESA's GMES Space Component Data Access (GSCDA) service is developed. This channel is set up to provide PROBA-V synthesis products S1-TOA, S1-TOC, and S10-TOC in the native format and in 1 km spatial resolution towards the GMES community. It is especially interesting for users who focus on long-term time series and want to continue their 1 km time series from SPOT-VEGETATION.

To serve the needs of the scientific user community, the retrieval of higher level (Level 4) products, such as basic biophysical variables, is also envisaged. Terrestrial essential climate variables, mainly leaf area index (LAI), fraction of absorbed photosynthetically active radiation (FAPAR), and surface albedo, will be made available to environmental and agricultural services aiming to assess biomass, carbon, and water fluxes. Therefore the Global Monitoring for Environment and Security (GMES) Land Service aiming to continuously monitor and forecast the status of land territories will be supported by the 'third party mission' PROBA-V. In brief, PROBA-V is meant to be part of the palette of sensors/platforms shaping the GMES Space Component.

5. Conclusion

As the intended gapfiller mission between SPOT-VEGETATION and the upcoming Sentinel-3 platform (Donlon et al. 2012), PROBA-V comfortably meets the requirements for a 1 km product, whereas for a 1/3 km product it maintains a performance consistent with that of SPOT-VEGETATION. Owing to constraints set by its smaller platform, on-board CCSDS compression is needed with an average compression ratio of 3.5, which has a noticeable impact on the radiometry of the 1/3 km product, but to an acceptable degree. The compression errors for the 1 km product are below the noise threshold. Spectral bands are not entirely similar, requiring careful cross-sensor calibration when comparing SPOT-VEGETATION data to PROBA-V. These differences are however sufficiently small to guarantee continuity for derived products such as the NDVI and NDWI.

Standard products for PROBA-V are similar to those of SPOT-VEGETATION, with the daily and 10 day synthesis being retained, and delivered for 1 km and 1/3 km

Table 12. Description of standard products and main data layers.

Product	Resolution	Image data	Auxiliary data
Level 1C	VNIR: 100–350 m SWIR: 200–700 m	Unprojected TOA reflectance [HDF5]	Sun viewing angles, raw grid [HDF5] Satellite viewing angles, raw grid [HDF5] Radiometric quality map, raw grid [HDF5]
S1-TOA	Both 1/3 km and 1 km	Projected TOA reflectance [HDF5]; NDVI [HDF5]	Sun viewing angles, mapped grid [HDF5] Satellite viewing angles, mapped grid [HDF5] Status Map, mapped grid [HDF5]
S1-TOC	Both 1/3 km and 1 km	Projected TOC reflectance [HDF5]; NDVI [HDF5]	Sun viewing angles, mapped grid [HDF5] Satellite viewing angles, mapped grid [HDF5] Status Map, mapped grid [HDF5]
S10-TOC	Both 1/3 km and 1 km	Projected TOC reflectance [HDF5]; NDVI [HDF5]	Sun viewing angles, mapped grid [HDF5] Satellite viewing angles, mapped grid [HDF5] Status Map, mapped grid [HDF5]

resolutions. As a double alternative for the VGT-P product, an S1-TOA product at 1/3 km and 1 km and a level 1C product at raw spatial resolution are provided. Standard products are provided by VITO's Web portal, which also allows requesting some customization options. In the frame of GMES, an additional channel is provided by ESA with its GSCDA portal (DAP Document 2011), which will provide the 1 km synthesis products. This is of primary interest for users with a focus on long-term 1 km time series.

The improved spatial resolution in the 1/3 km product and in the raw resolution level 1C product is the essential feature that has changed compared to SPOT-VEGETATION specifications. The 1/3 km product places it in the range of MODIS and the derived VIIRS mission (Townshend and Justice 2002), although with a more limited scope of spectral bands. Observations of the central camera at 100 m raw resolution in the Level 1C product will not have guaranteed radiometric performances in terms of SNR, and therefore considered as 'science grade' products. The improved spatial resolution can be of special interest for novel applications (Roumenina et al. 2012; Azzi et al. 2011; Inglada 2011).

Acknowledgements

The authors acknowledge the contribution of the teams from Qinetiq Space, OIP, Spacebel, ACS, and Trasy. This work was supported by Belspo and ESA (PROBA-V contract 091670).

Furthermore, we wish to honour the memory of Gilbert Saint, one of the founders of the VEGETATION mission, who passed away on 10 May 2012. His experience during his years at CNES and GEOSYS made him an invaluable asset in his role as consultant for the PROBA-V mission. He made core contributions for the image quality of the PROBA-V mission (and thus the work of this article), and in his role as scientific secretary of the PROBA-V IUC he has been a driving force for the other scientific work found in this issue of *International Journal of Remote Sensing*. He will be remembered for his valuable legacy and his conscientious way of working.

References

- Aschbacher, J., and M. P. Milagro-Perez. 2012. "The European Earth Monitoring (GMES) Programme: Status and Perspectives." *Remote Sensing of Environment* 120: 3–8.
- Azzi, A., I. Manakos, C. Kalaitzidis, M. Schardt, and H. Gallaun. 2011. "PROBA-V Performance Assessment for Forest Cover Mapping over the Atlantic Biogeographical Region of Europe." *EARSeL eProceedings* 10 (2): 166–173.
- Bermyn, J., and C. Dorn. 2008. "PROBA Spacecraft Family: Small Mission Solutions for Emerging Applications." In *Small Satellites for Earth Observation: Selected Contributions*, edited by R. Sandau, H.-P. Röser, and A. Valenzuela, 67–76. New York: Springer.
- CCSDS Secretariat. 2005. *CCSDS: Image Data Compression, Recommendation for Space Data System Standards. CCSDS 122.0-B-1, Blue Book Issue 1*. Washington, DC: CCSDS Secretariat.
- Cohen, J. 1968. "Weighted Kappa: Nominal Scale Agreement Provision for Scaled Disagreement or Partial Credit." *Psychological Bulletin* 70 (4): 213–220.
- DAP Document. 2011. "GMES Space Component Data Access Portfolio: Data Warehouse 2011–2014." GMES-PMAN-EOPG-TN-11-0006, v2.5. http://gmesdata.esa.int/web/gsc/dap_document
- Donlon, C., B. Berruti, A. Buongiorno, M.-H. Ferreira, P. Femenias, J. Frerick, P. Goryl, U. Klein, H. Laur, C. Mavrocordatos, J. Nieke, H. Rebhan, B. Seitz, J. Stroede, and R. Sciarra. 2012. "The Global Monitoring for Environment and Security (GMES) Sentinel-3 Mission." *Remote Sensing of Environment* 120: 37–57.
- Fiethe, B., H. Michalik, C. Dierker, B. Osterloh, and G. Zhou. 2007. "Reconfigurable System-On-Chip Data Processing Units for Space Imaging Instruments." In *Proceedings of the Conference on Design, Automation and Test in Europe*. San Jose, CA: EDA Consortium, 977–982.
- Fougnie, B., G. Bracco, B. Lafrance, C. Ruffel, O. Hagolle, and C. Tinel. 2007. "PARASOL in-Flight Calibration and Performance." *Applied Optics* 46 (22): 5435–5451.
- Fougnie, B., P. Henry, A. Morel, D. Antoine, and F. Montagner. 2002. "Identification and Characterization of Stable Homogeneous Oceanic Zones: Climatology and Impact on in-

- Flight Calibration of Space Sensor over Rayleigh Scattering.” Proceedings of Ocean Optics XVI, Santa Fe, NM, November 18–22.
- Govaerts, Y. M., S. Sterckx, and S. Adriaensen. 2013. “Use of Simulated Reflectances over Bright Desert Target as an Absolute Calibration Reference.” *International Journal of Remote Sensing* 4 (6): 523–531.
- Hagolle, O., P. Goloub, P. Y. Deschamps, H. Cosnefroy, X. Briottet, T. Bailleul, J. M. Nicolas, F. Parol, B. Lafrance, and M. Herman. 1999. “Results of POLDER in-Flight Calibration.” *IEEE Transactions on Geoscience and Remote Sensing* 37 (3): 1550–1566.
- Hagolle, O., J. M. Nicolas, B. Fougnie, F. Cabot, and P. Henry. 2004. “Absolute Calibration of VEGETATION Derived from an Interband Method Based on the Sun Glint over Ocean.” *IEEE Transactions on Geoscience and Remote Sensing* 42 (7): 1472–1481.
- Henry, P., and A. Meygret. 2001. “Calibration of VEGETATION Cameras On-board SPOT4.” Proceedings of VEGETATION 2000 Conference, CNES-Toulouse & JRC – ISPRA, Belgirate, April 3–6.
- Inglada, J. 2011. “Low and High Spatial Resolution Time Series Fusion for Improved Land Cover Map Production.” In *6th International Workshop on the Analysis of Multi-temporal Remote Sensing Images (Multi-Temp)*, 77–80. New York: IEEE Publishing.
- Kotchenova, S.Y., E. Vermote, R. Matarrese, and F.J. Klemm Jr. 2006. “Validation of a Vector Version of the 6S Radiative Transfer Code for Atmospheric Correction of Satellite Data. Part I: Path Radiance.” *Applied Optics* 45 (26): 6762–6774.
- Lisens, G., P. Kempeneers, F. Fierens, and J. Van Rensbergen. 2000. “Development of Cloud, Snow, and Shadow Masking Algorithms for VEGETATION Imagery.” In *Proceedings of Geoscience and Remote Sensing Symposium, IGARSS 2000*, vol. 2, 834–836. New York: IEEE Publishing.
- Livens, S., and R. Kleihorst. 2009. “Compression of Remote Sensing Images for the PROBA-V Satellite Mission.” In *Advanced Concepts for Intelligent Vision Systems, 11th International Conference (ACIVS)*, 577–586. Bordeaux: France.
- Maisongrande, P., B. Duchemin, and G. Dedieu. 2004. “VEGETATION/SPOT: An Operational Mission for the Earth Monitoring; Presentation of New Standard Products.” *International Journal of Remote Sensing* 25 (1): 9–14.
- Mica, S., L. Galli, G. Duhoux, S. Livens, A. Giustiniani, J. C. Dries, J. Zender, and S. Santandrea. 2012. “PROBA-V Geometric Calibration Processing.” Paper presented at *IEEE International Geoscience and Remote Sensing Symposium*, Munich, July 22–27.
- Michalik, H., S. Wolter, M. Von Der Wall, L. Hinsenkamp, B. Penne, and R. Rathje. 2006. “High-Rate CCSDS Formatter/Encoder Plus IDEA Encryptor as a Single-Chip Solution.” *Acta Astronautica* 58 (12): 642–647.
- Roumenina, E., L. Filchev, V. Vassilev, P. Dimitrov, G. Jeley, G. Stancalie, E. Savin, and D. Mihailescu. 2012. “Comparative Analysis of Crop Maps for Chosen Test Areas on the Territory of Bulgaria and Romania Using Simulated Proba-V and Spot Vegetation Data.” *EARSeL eProceedings* 11 (2): 155–160.
- Saint, G. 1995. “VEGETATION Onboard SPOT4: Mission Specifications – Version 3. VGT/PS/940518/1.” Accessed January 29, 2014. www.vgt.vito.be/pages/VegetationSystem/mission.htm
- Schyns, J. C. 2010. “The PROBA-V Mission: Data Continuity for Daily Global Vegetation Monitoring.” In *Proc/30th EARSeL Symposium: Remote Sensing for Science, Education and Culture*. Paris: Earsel, 635–640.
- Smits, P. C., S. G. Dellepiane, and R. Schowengerdt. 1999. “Quality Assessment of Image Classification Algorithms for Land-Cover Mapping: A Review and Proposal for a Cost-Based Approach.” *International Journal of Remote Sensing* 20: 1461–1486.
- Sterckx, S., S. Adriaensen, S. Livens, W. Dierckx, and I. Reusen. 2011. “PROBA-V IQC: Radiometric Cal/Val Activities after Launch.” Presentation presented at 23rd meeting of CEOS Working Group on Calibration and Validation, subgroup Infrared and Visible Optical Systems (IVOS-23), Toulouse, June 22.
- Sterckx, S., I. Benhadj, G. Duhoux, S. Livens, W. Dierckx, E. Goor, S. Adriaensen, W. Heyns, K. Van Hoof, G. Strackx, K. Nackaerts, I. Reusen, T. Van Achteren, J. Dries, T. Van Roey, K. Mellab, R. Duca, and J. Zender. 2014. “The PROBA-V Mission: Image Processing and Calibration.” *International Journal of Remote Sensing* 35 (7): 2565–2588.
- Sterckx, S., S. Livens, and S. Adriaensen. 2013. “Rayleigh, Deep Convective Clouds and Cross Sensor Desert Vicarious Calibration Validation for the PROBA-V Mission.” *Transactions on Geoscience and Remote Sensing* 51 (3): 1437–1452.

- Swinnen, E., and F. Veroustraete. 2008. "Extending the SPOT-VEGETATION NDVI Time Series (1998–2006) Back in Time with NOAA-AVHRR Data (1985–1998) for Southern Africa." *IEEE Transactions on Geoscience and Remote Sensing* 46 (2): 558–572.
- Townshend, J. R. G., and C. O. Justice. 2002. "Towards Operational Monitoring of Terrestrial Systems by Moderate-Resolution Remote Sensing." *Remote Sensing of Environment* 83 (1–2): 351–359.
- Trischenko, A. P. 2009. "Effects of Spectral Response Function on Surface Reflectance and NDVI Measured with Moderate Resolution Satellite Sensors: Extension to AVHRR NOAA-17, 18 and METOP-A." *Remote Sensing of Environment* 113: 335–341.
- Turkowski, K., and S. Gabriel. 1990. "Filters for Common Resampling Tasks." In *Graphics Gems I*, edited by A. S. Glassner, 147–165. Boston, MA: Academic Press.
- Vermote, E., and Y. Kaufman. 1995. "Absolute Calibration of AVHRR Visible and Near Infrared Channels Using Ocean and Cloud Views." *International Journal of Remote Sensing* 16: 2317–2340.
- Vermote, E., R. Santer, P. Y. Deschamps, and M. Herman. 1992. "In-Flight Calibration of Large Field-of-View Sensors at Short Wavelengths Using Rayleigh Scattering." *International Journal of Remote Sensing* 13 (18): 3409–3429.
- Versluys, J., D. Kendall, W. Moelans, D. Mollet, P. Holbrouck, D. Vrancken, M. Taccola, and M. Francois. 2012. "The Vegetation Instrument: A Small Scale High Performance Earth Observation Instrument." Paper presented at Small Satellite Systems and Services – The 4S Symposium, Portorož, Slovenia, June 4–8.
- Vrancken, D., D. Gerrits, K. Mellab, and S. Santandrea. 2012. "PROBA-V: A Multi-Spectral Earth Observation Mission Based on a PROBA Platform – Status Update." Paper presented at Small Satellite Systems and Services – The 4S Symposium, Portorož, Slovenia, June 4–8.